Journal of Magnetic Resonance 303 (2019) 121–127

Contents lists available at ScienceDirect

Journal of Magnetic Resonance

journal homepage: www.elsevier.com/locate/jmr

High-resolution MRI of kidney microstructures at 7.05 T with an endo-colonic Wireless Amplified NMR detector

Xianchun Zeng [a,e], Shuangtao Ma [b], John M. Kruger [c], Rongpin Wang [a], Xiaobo Tan [d], Chunqi Qian [e,*]

[a] Department of Radiology, Guizhou Provincial People's Hospital, Guiyang, China
[b] Department of Medicine, Michigan State University, East Lansing, MI, USA
[c] Veterinary Medical Center, Michigan State University, East Lansing, MI, USA
[d] Department of Electrical and Computer Engineering, Michigan State University, East Lansing, MI, USA
[e] Department of Radiology, Michigan State University, East Lansing, MI, USA

ARTICLE INFO

Article history:
Received 18 February 2019
Revised 19 April 2019
Accepted 21 April 2019
Available online 25 April 2019

Keywords:
In situ amplification
Medullary rays
Hemodynamic responses imaging
Endoscopic detector

ABSTRACT

To map the hemodynamic responses of kidney microstructures at 7.05 T with improved sensitivity, a Wireless Amplified NMR Detector (WAND) with cylindrical symmetry was fabricated as an endoluminal detector that can convert externally provided wireless signal at 600.71 MHz into amplified MR signals at 300.33 MHz. When this detector was inserted inside colonic lumens to sensitively observe adjacent kidneys, it could clearly identify kidney microstructures in the renal cortex and renal medullary. Owing to the higher achievable spatial resolution, differential hemodynamic responses of kidney microstructures under different breathing conditions could be individually quantified to estimate the underlying correlation between oxygen bearing capability and local levels of oxygen unsaturation. The WAND's ability to map Blood Oxygen Level Dependent (BOLD) signal responses in heterogeneous microstructures will pave way for early-stage diagnosis of kidney diseases, without the use of contrast agents for reduced tissue retention and toxicity.

1. Introduction

There is an unmet need for non-invasive monitoring of kidney physiology in focal regions. Renal diseases often start from regional dysfunction in glomerular filtration, compensated by hyperfiltration in remaining nephrons. Therefore, circulatory or urinary biomarkers are often insensitive to focal deficits until substantial renal function is lost. Compared to other noninvasive imaging modalities that cannot simultaneously provide good spatial resolution and tissue-dependent signal contrast, MRI (if given adequate sensitivity) can in principle provide important insights into renal microcirculation that is closely related to focal physiology. For example, blood-oxygen-level-dependent (BOLD) signal changes in MR images can map the kidney's oxygen homeostasis under altered physiological conditions [1–3]. Although BOLD MRI can map tissues' hemodynamic responses without the potential side effects of exogeneous contrast agents [4], such as tissue retention or toxicity, its successful application in brains [5,6] and muscles [7] doesn't directly translate to consistent results in kidneys. Some studies found transverse relaxivity changes in kidneys' overall layers during hyperoxia breathing [8], but others did not [9,10]. Such inconsistent results are partly due to the insufficient sensitivity and resolution enabled by conventional external MR detectors that cannot identify differential hemodynamic responses of kidney microstructures, including the glomeruli and renal tubules that serve the vital function of plasma filtration and filtrate reabsorption. Prior studies using lower-resolution images could only characterize average hemodynamic responses, concealing important information about their differences.

To improve MRI detection sensitivity for deep-lying renal tissues, smaller coils implanted in closer proximity to the region of interest were used for larger signal responses to electromotive forces induced by precessing nuclei spins [11,12]. Although these implanted detectors were originally developed with wired connections, mutual inductive coupling [13–17] was later used to wirelessly transmit MR signals for better operation convenience and reduced risk of chronic infection. However, wireless inductive coupling can be inefficient when the implanted detector is separated from the body's surface by a distance much larger than the detector's own dimension. To improve signal transmission efficiency of inductive coupling, a Wireless Amplified NMR Detector (WAND) was later developed to simultaneously amplify locally detected MR signals, reducing sensitivity loss during signal transmission.

* Corresponding author at: 846 Service Rd, East Lansing, MI, 48824, USA.
E-mail address: qianchu1@msu.edu (C. Qian).

https://doi.org/10.1016/j.jmr.2019.04.014
1090-7807/

Just like "passive" inductive couplers, the "amplified" WAND was initially used as an implantable detector mounted on the surface of kidney, but with greatly improved sensitivity to identify individual nephrons *in vivo* [18,19]. Later, the WAND was re-engineered with cylindrical symmetry for non-surgical use inside the digestive tract [20–22], to better image aorta walls or heterogenous tumors. In this work, we are going to extend the non-surgical application of the WAND into kidney microstructure imaging *in vivo*, an application scenario primarily addressed by surgically implanted MR detectors before. Utilizing the proximity between the colon and the kidney, this endo-cavity detector can sensitively identify heterogenous microstructures in different kidney layers. By sequentially exposing the rat to 50%–O_2 and 96%–O_2 breathing conditions, the differential BOLD signal response of vascular-rich and vascular-sparse regions can be utilized to evaluate local oxygen delivery that is correlated with capillary blood flow. Because renal hypoxia is a common etiological factor that originates locally, the ability to detect differential hemodynamic responses of renal microstructures will enable early diagnosis of renal abnormities based on O_2 delivery deficiency, without contrast agent induced toxicity.

2. Materials and methods

2.1. Detector operation principle

The WAND was advantageous over conventional signal amplifiers because it could operate without batteries or wires and is thus easier to deploy inside the body. It can non-surgically enter the GI tract, approach deep-lying tissues and sensitively observe them across the luminal walls. Unlike wireless chargers, the WAND could directly convert wirelessly harvested energy into amplified MR signals [23], without the need for rectifiers that would require extra space. As shown in Fig. 1, the WAND could be implemented as a cylindrical resonator mounted on a 2.4-mm diameter polyurethane cylinder, with two identical conductor legs interlaced with two identical conductor end-rings. A continuous center ring was optionally introduced to neutralize excessive charge accumulated across end-ring diodes. The 0.5-mm wide conductor legs and rings are etched on copper-clad polyimide. Both end-rings were split by a pair of Schottky diodes (BAS3005A, Infineon, Neubiberg, Germany) connected in a head-to-tail configuration. The vertical legs, along with the diodes' junction capacitance (C) at zero-bias voltage, create the transverse resonance mode that was sensitive to MR signal input at the Larmor frequency ω_1. Meanwhile, the two identical split end rings created a longitudinal resonance mode that was sensitive to an electromagnetic pumping field at the frequency ω_3, which was wirelessly provided by a single-turn pumping loop (red) wrapped around the rat. By making the pumping frequency ω_3 to be 600.71 MHz, which was approximately twice the Larmor frequency ω_1 of 300.33 MHz at 7.05 T, the nonlinear capacitance (C) of end-ring diodes could facilitate efficient energy transfer from the longitudinal mode to the transverse resonance mode.

During the slice excitation period, about 10 W of power was applied on an external transmit coil (not shown for brevity) to excite nuclei spins. This strong excitation field would transiently couple with the transverse resonance mode of the WAND to induce large voltage modulations across all diodes. During each half of the modulation cycle, at least two diodes were turned on to detune the WAND from the Larmor frequency, thus decoupled the WAND from the excitation field. During the subsequent signal reception period, a milliwatts-level pumping power was applied on the (red) pumping loop that continuously coupled with the longitudinal resonance mode of the WAND, modulating all end-ring diodes in a synchronized way. As a result, a weak MR signal at the Larmor frequency ω_1 (green arrow) could mix with the much larger pumping signal at ω_3 (red arrow) to create an amplified output at the idler frequency $\omega_2 = \omega_3 - \omega_1$ (pink arrow). This amplified output at ω_2 (pink circular arrow) could mix back with the pumping signal at ω_3 (red arrow) to create a second amplified output at ω_1 (cyan arrow), which could be detected by a standard external coil. In our case, $|\omega_2 - \omega_1|$ was set to at least 50 kHz, which was slightly larger

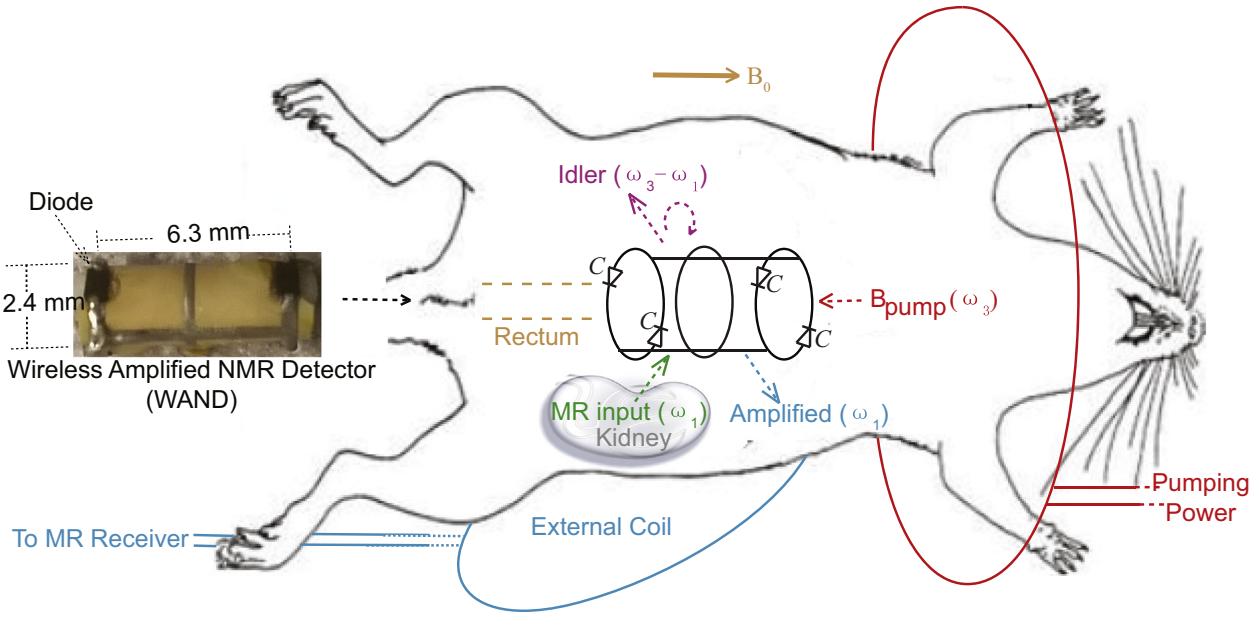

Fig. 1. A simple cylindrical detector inside the digestive tract can sensitively detect and simultaneously amplify MR signals emitted from deep-lying tissues. As shown in the picture (left) and the schematic diagram (right), the WAND has four diodes (BAS3005A, Infineon) equally distributed on its two end rings. It has a longitudinal resonance mode to receive pumping signal and a homogeneous transverse resonance mode to receive weak MR signals. The pumping loop (red) provides magnetic energy into the WAND through wireless coupling. Aided by multi-stage signal mixing, this pumping energy is converted to amplified MR signals that are re-emitted by the WAND for signal reception in the external coil (cyan). For better operation stability, the WAND has an additional ring placed in its cylindrical center to neutralize accumulated charge across end-ring diodes. (For interpretation of the references to colour in this figure legend, the reader is referred to the web version of this article.)

than the imaging bandwidth, so that the amplified MR signal at ω_1 would not interfere with the idler signal at ω_2. Compared to external detection, the WAND in its passive state had up to 3-fold gain in normalized intensity for regions with at least one diameter separation from its cylindrical surface; active amplification could provide an additional 3-fold gain. The WAND's favorable feature of wireless operation and excitation-induced decoupling would also make it safer than conventional interventional detectors, by eliminating hard-wired connections that could effectively couple with the strong excitation field due to wavelength effect. The negligible heating effect of the WAND was experimentally confirmed by the non-measurable temperature rise on a rectal probe inserted nearby during MR experiments. Finally, because the WAND's center ring is parallel to the B_1 excitation field or the precessing magnetic moment, this center ring would create negligible impact on the detector's cylindrical symmetry, as confirmed by the phantom image, the sensitivity-gain profile and the excitation angle map [45] shown in Supplemental Figures.

Supplementary data associated with this article can be found, in the online version, at https://doi.org/10.1016/j.jmr.2019.04.014.

2.2. In vivo imaging

All animal experiments were approved by the Institutional Animal Care and Use Committee at MSU, in accordance to guidelines established by the U.S. National Academy of Sciences. Four male SD rats weighing ~250 g were imaged inside a 7.05-T magnet equipped with a 77-mm bore volume coil and an AVANCE III console (Bruker Biospin, Billerica, MA). Each rat was anesthetized with 1.5–2% isoflurane at a flow rate of 0.9 mL/min. Its respiratory rate was monitored by a pneumatic pillow sensor (SA Instruments, Stony Brook, NY) and its heart rate monitored by three electrodes (two inserted in its front paw and one in its rear paw), as anesthesia was fine adjusted to maintain an average respiration rate at 50 breaths/min and a heart rate at 350 beats/min. The blood oxygen saturation level was maintained above 96%, as monitored by a pulsed oximetry sensor clamped on the empty rear paw. To provide signal interface with the MRI console, a rectangular surface coil with a dimension of 28×28 mm^2 was placed beneath the left kidney and used as the external detector whose dimension was chosen to be slightly larger than the depth of the kidney's medial surface. For sensitivity enhancement, the WAND was inserted into the lower digestive tract, whose insertion depth was manually adjusted by a connection rod until the WAND's cylindrical tip was levelled with the cranial extremity of the left kidney as confirmed by low-resolution localizer images (that were acquired using TE/TR = 2.9/138 ms, Flip Angle = 35°, FOV = 6×6 cm^2, matrix size = 256×256, slice thickness = 1 mm, Number of Acquisition = 1). This position adjustment procedure would ensure the WAND to reproducibly observe similar kidney regions in each rat. Subsequently, higher-resolution images of kidney microstructures were acquired in the absence and presence of pumping power, using Gradient Refocused Echo sequence and the following acquisition parameters: TE/TR = 20/1200 ms, Flip Angle = 60°, FOV = 25.6×25.6 mm^2, matrix size = 256×256, in-plane resolution = 0.1 mm, slice thickness = 0.8 mm, Number of Acquisition (NA) = 1. This large enough slice thickness and the large enough TE (at 7.05 T) were chosen to highlight the signal contrast between vascular-rich (grayer) and vascular-sparse (brighter) regions. To avoid motion artifacts, respiratory gating was used to acquire images during static intervals. To evaluate the BOLD effect in the renal cortex, amplified images were first acquired under 50%–O_2 breathing to identify pixels with lower intensity from their surroundings. Images acquired under 50%–O_2 breathing were then divided by the those acquired under 96%–O_2 breathing to quantify differential signal responses of individual pixels.

2.3. Image processing and statistical analysis

All images were normalized against the standard deviation of their respective noise floors. Kidney regions in Fig. 2 that were directly observed by the external detector were compared for normalized intensity to those regions observed by the WAND in the absence and presence of pumping power. To quantify the distribution of bright bundles that were clearly visible in the amplified images, the intersection angles between adjacent bundles were measured and averaged across the enhanced regions of renal medulla. To identify the underlying correlation between differential hemodynamic responses and microstructure signal heterogeneities, regression analysis was performed over individual pixels in the renal cortex, with details procedures summarized below. All measurement results were presented as the mean ± s.e.m.

3. Results

Fig. 2a showed the low-resolution localizer image acquired to identify the position of the WAND, whose top edge was adjusted by the connection rod to approximately level with the cranial extremity of the kidney. Fig. 2b was a longitudinal image slice with a ~3.5-mm distance separation from WAND's cylindrical surface to pass through the kidney's Inner Medulla (IM). Acquired in the absence of pumping power, Fig. 2b could identify the four kidney layers from outer to inner, i.e. the cortex, the Outer Strip of Outer Medulla (OSOM), the Inner Strip of Outer Medulla (ISOM) and the inner medulla. But because of the relatively large distance separation between the renal medulla and the rat's skin, none of the medulla layers showed clearly identifiable internal structures, except in the upper half of the kidney where bundle structures were vaguely visible due to their proximity to the passive WAND placed inside the nearby colon, leading to ~2.4-fold gain ($\delta = 0.4$) over external detection. With the pumping power turned on, white bundles in the renal medulla were clearly identified to separate from each other by an angle of 10.1 ± 1.2° (Fig. 2c). These white bundles were highlighted to have another ~3-fold gain ($\delta = 0.5$) in normalized intensity over passive detection, showing better connectivity and sharper contrast from their surroundings. In Fig. 2c, the approximate distance separation of 0.2 mm between adjacent grayer bundles could be clearly identified in the 0.8-mm slice, because the 20-ms echo time at 7.05 T would induce large enough signal dephasing in the otherwise brighter background. Fig. 2d and e showed the longitudinal images acquired across the outer medullar in a different rat, demonstrating the WAND's reproducible capability for microstructural imaging in different kidney layers.

In addition to high-resolution structural imaging, the WAND could also map differential hemodynamic responses of kidney microstructures under altered inhalation conditions. As shown in an image slice passing through the renal cortex of another rat (Fig. 3a1), there were multiple black dots with much lower intensities than their surroundings. For example, the intensity valley in the center of the 1D plot (Fig. 3a2) had ~30% the height of its left-shoulder peaks. When the inhaled gas was switched from 50% O_2 to 96% O_2, the valleys' height increased by ~2.0-fold ($\delta = 0.4$), whereas the heights of their shoulder peaks in Fig. 3b2 increased by ~1.4-fold ($\delta = 0.1$). The differential intensity responses of peaks and valleys confirmed the larger hemodynamic responses of regions with lower intensity in Fig. 3a1. To quantify the differential hemodynamic responses of individual pixels over the cortex region, we calculated the **M**edium-hyper**O**xia-**R**atio (**MOR**) of each image pixel, by dividing the sensitivity-normalized image acquired under 50%–O_2 breathing with that acquired under 96%–O_2 breath-

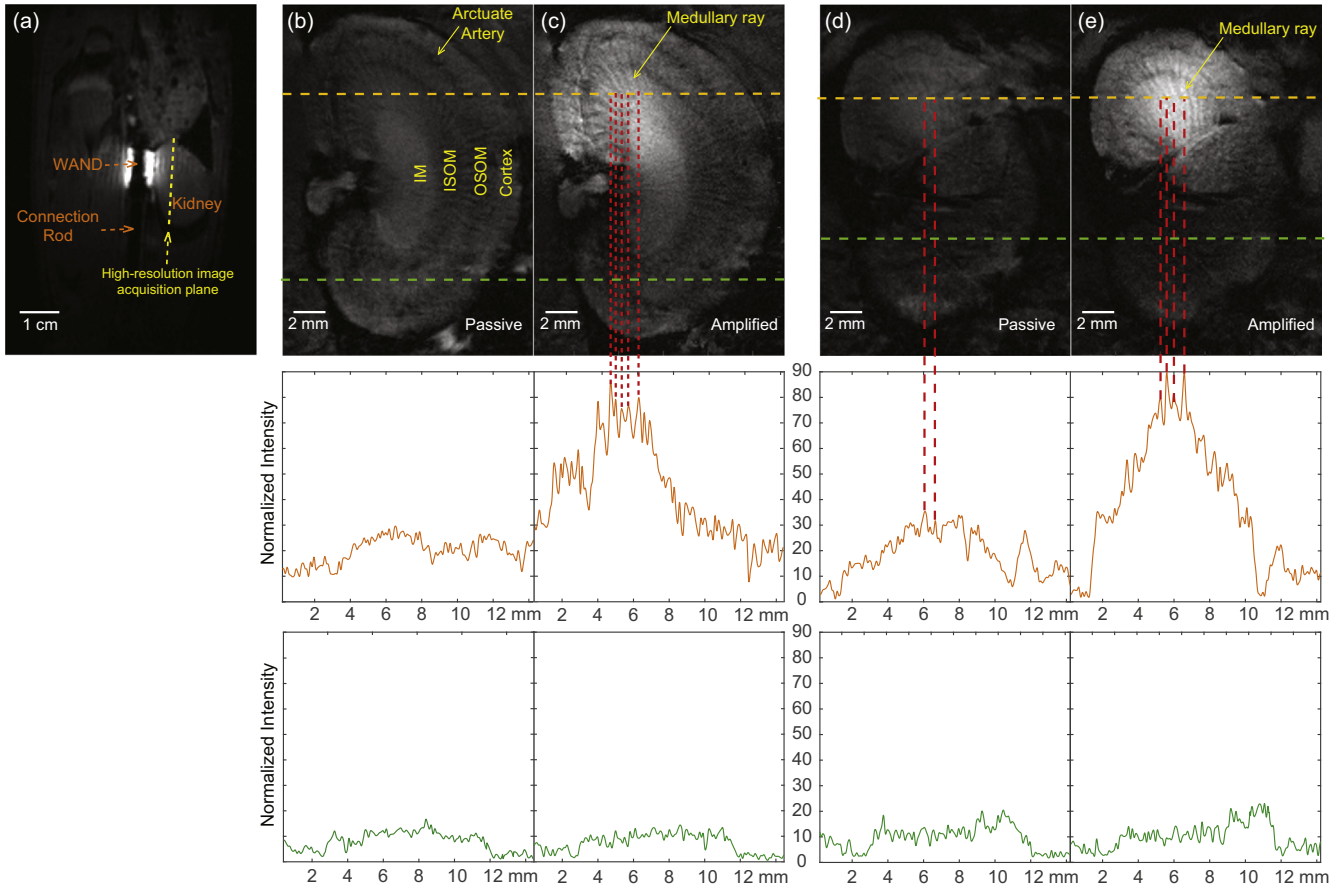

Fig. 2. (a) A low-resolution image slice passing through both the cylindrical axis of the WAND and the cranial edge of the kidney, acquired using TE/TR = 2.9/138 ms, Flip Angle = 35°, FOV = 6 × 6 cm^2, matrix size = 256 × 256, slice thickness = 1 mm, Number of Acquisition = 1. (b) A high-resolution image slice acquired parallel to the WAND's cylindrical surface to show microstructures inside the inner medulla, using Gradient Refocused Echo (GRE) sequence and TE/TR = 20/1200 ms, Flip Angle = 60 deg, In-plane resolution = 0.1 mm, slice thickness = 0.8 mm, Number of Acquisition = 1. The normalized intensity is plotted along the green dashed line in the bottom half of the image and the orange dashed line in the upper half of the image to respectively demonstrate the limited sensitivity of external detection and passive inductive coupling. (c) A longitudinal slice acquired by the WAND in the presence of pumping power, using the same parameters as (b). This sensitivity-enhanced image has bundles of bright stripes in the renal medulla that are interlaced with gray stripes. (d) and (e) are longitudinal images acquired across the outer medulla of another rat in the absence and presence of pumping power, demonstrating the reproducible signal enhancement patterns of kidney microstructures under amplification. (For interpretation of the references to colour in this figure legend, the reader is referred to the web version of this article.)

ing: **MOR** = I_{med}/I_{hyper}. To identify the local image contrast of each pixel under 50%–O_2 breathing, we also calculated the **R**elative **I**ntensity (**RI**) of each pixel by dividing its signal intensity with the smoothed intensity evaluated over a contiguous region around that pixel. The size of this contiguous region was 7 × 7 pixels, which was slightly larger than the average distance separation between adjacent black spots. We then plotted **MOR** with respect to **RI** for each pixel and found a positive correlation between these two variables (Fig. 3c). The differential hemodynamic responses of heterogeneous microstructures were again verified in another rat under 50%–O_2 (Fig. 3d1) and 96%–O_2 (Fig. 3e1) breathing, where the positive correlation between hyperoxia-induced signal response (as represented by **MOR**) and signal heterogeneity (as represented by **RI**) was reproducibly identified (Fig. 3f). More measurement results for different rats were summarized in Table 1.

4. Discussion

Normally, MR microimaging of kidneys are primarily performed *ex vivo* [24–30]. For *in vivo* microimaging, cryogenic coils have been used to map blood perfusion in mouse kidneys with good spatial resolution [31,32], although coil cooling works better for mouse kidneys near surface regions where sample noise is smaller compared to coil noise [33,34]. To perform microimaging on rat kidneys in deeper regions where sample noise [35] dominate, the reduced image sensitivity can be partially compensated by the use of targeted contrast agents, and the image quality of glomeruli distribution [36–38] can be further improved by repetitive acquisition.

In our work, a cylindrically symmetric WAND operating at room temperature is fabricated and non-surgically inserted into rats' rectums to observe deep-lying regions of adjacent kidney from colonic lumens. The enhanced sensitivity offered by this WAND detector has provided additional possibilities to better observe the endogenous signal contrasts of kidney micro-structures, without the need for exogenous agents or repetitive acquisition. For example, the interlaced patterns in the renal medulla can be clearly observed by the actively amplified detector (Fig. 2c, e). These interlaced patterns are consistent with histological results reported previously [39–42], where bundles of vasa recta are interlaced with medullary rays supplied by capillary plexus.

As another example, the WAND can clearly identify hemodynamic responses of individual pixels at high spatial resolution, based on the Blood-Oxygen-Level-Dependent (BOLD) modulation of signal intensity under altered breathing conditions. The black spots in Fig. 3a1 and 3d1 have higher signal response to hyperoxia breathing than their surroundings. These larger hemodynamic

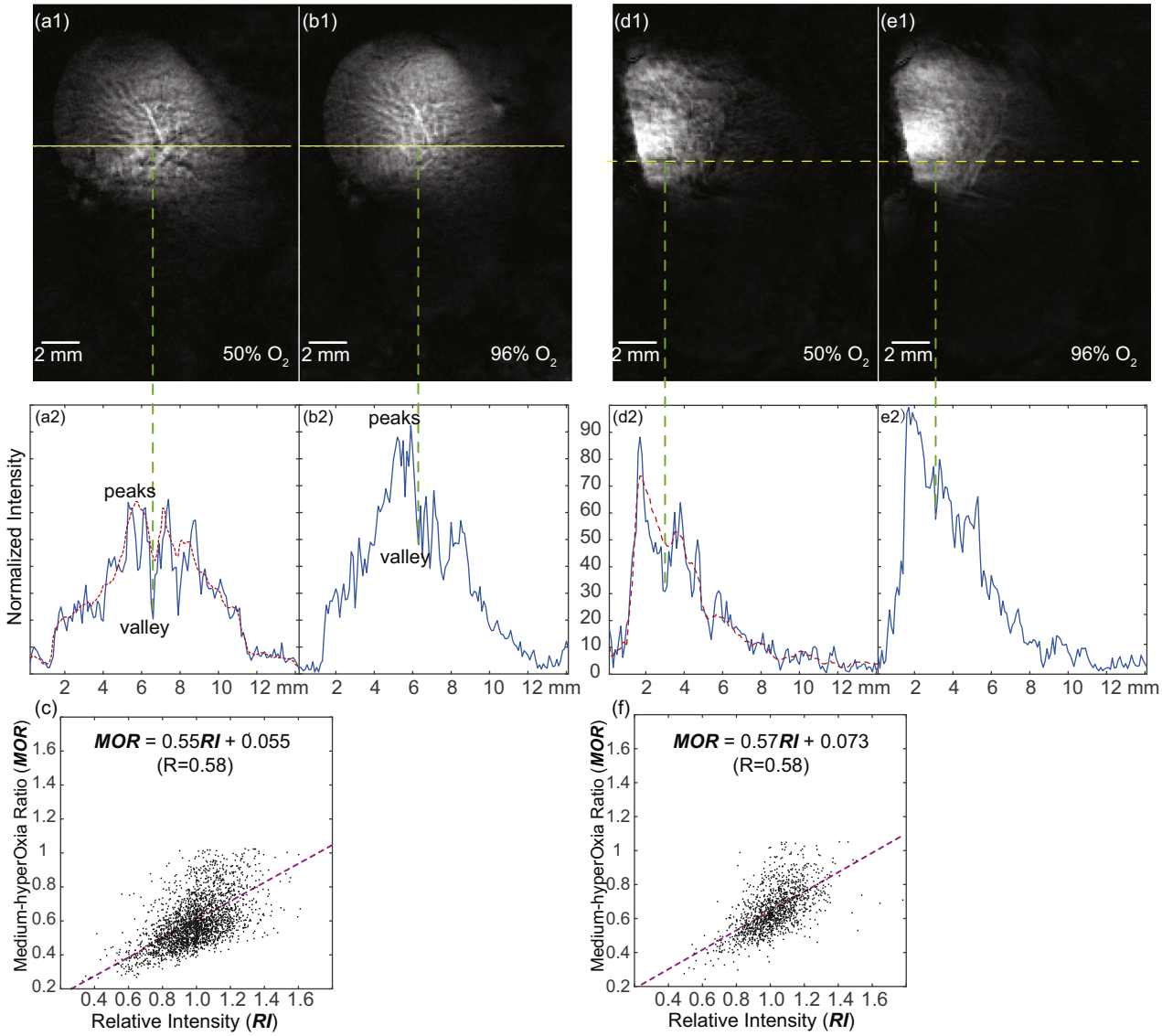

Fig. 3. High-resolution hemodynamic response images of micro vessels. (a1) is a sensitivity-enhanced image acquired across the renal cortex when the rat was inhaling 50% O_2, using TE/TR = 20/1200 ms, Flip Angle = 60 deg, 0.1-mm In-plane resolution, 0.8-mm slice thickness. The normalized intensity profile along the yellow-dashed line in (a1) is plotted in (a2). The **R**elative **I**ntensity (**RI**) is obtained by dividing the intensity of each pixel with the intensity of the smoothed profile (red dotted line). For each pixel in the image, a smaller **RI** is indicative of a higher level of oxygen unsaturation. (b1) is the same image acquired on the same kidney region when the rat was inhaling 96% oxygen. (b2) is the corresponding normalized intensity profile with greatly decreased signal contrast between vascular-rich and vascular-sparse regions. (c) shows the positive correlation between the **M**edium-hyper**O**xia **R**atio (**MOR**) and the **R**elative **I**ntensity (**RI**) in the cortex of a healthy kidney. The **MOR** of each pixel is obtained by dividing the sensitivity-normalized image acquired under 50%–O_2 breathing with that acquired under 96%–O_2 breathing. A lower **MOR** is indicative a higher O2-bearing capacity. (d) and (e) are images acquired on another rat using the same protocol, when the rat was breathing 50% O_2 and 96% O_2 respectively. (f) shows the reproducible correlation between **MOR** and **RI** for this different rat. (For interpretation of the references to colour in this figure legend, the reader is referred to the web version of this article.)

Table 1
Summary of image results in different rats.

Rat #	Enhancement factor	Inter-stripe angle	Hyperoxia response v.s. Image contrast
1	8.2 ± 1.4	10.1 ± 1.2°	***MOR*** = 0.56 ***RI*** + 0.068 (R = 0.60)
2	7.3 ± 1.5	9.8 ± 1.0°	***MOR*** = 0.58 ***RI*** + 0.060 (R = 0.57)
3	7.8 ± 1.3	10.3 ± 1.4°	***MOR*** = 0.55 ***RI*** + 0.055 (R = 0.58)
4	8.4 ± 1.2	10.0 ± 1.1°	***MOR*** = 0.57 ***RI*** + 0.073 (R = 0.58)

For each rat listed in column 1, the signal enhancement factor for its medulla region is listed in column 2. The intersection angle between adjacent medullary rays is evaluated across the entire medulla and listed in column 3. Column 4 shows the correlation between pixels' hemodynamic responses under hyperoxia breathing and the relative intensity of individual pixels in the renal cortex.

responses could be explained by the lower oxygen saturation of these spots under 50%–O_2 breathing. Meanwhile, 96% O_2 inhalation will increase the oxygen pressure in these spots through increased oxygen delivery in arterial blood and increased arteriovenous oxygen shunting, leading to increased T_2^* and increased signal intensity. In order to quantify the hemodynamic responses of heterogeneous microstructures while removing baseline variations, we calculated the Medium-hyperOxia Ratio (**MOR**) as the signal intensity ratio under 50%–O_2 and 96%–O_2 breathing: smaller **MOR** indicates higher levels of oxygen bearing capability, while larger **MOR** indicates lower levels of oxygen bearing capability. To depict signal heterogeneity of kidney microstructures under 50%–O_2 breathing, the **R**elative **I**ntensity (**RI**) of each pixel is calcu-

lated by dividing its signal intensity with the local average. A positive relation is found between **MOR** and **RI**, which can probably be attributed to the proportionality between O_2-bearing capability and the local level of deoxyhemoglobin. Of course, further study is needed to understand this positive correlation. Although BOLD-MRI has previously been used to map oxygen levels in overall layers [43] of kidney (i.e. renal cortex, outer medulla and inner medulla), due to the relatively low detection sensitivity of external detectors, conventional BOLD-MRI was acquired at a spatial resolution that couldn't discern the differential hemodynamic responses of kidney microstructures within overall kidney layers. With the enhanced sensitivity delivered by the WAND, it is possible to individually identify the differential BOLD responses of individual pixels, which are closely related local changes in oxygenation.

Because renal hypoxia is a common etiological factor that starts from localized regions, the ability to identify distinct hemodynamic responses of kidney microstructures will pave the way for early diagnosis of kidney diseases. Without administration of exogenous contrast agents, high-resolution hemodynamic response imaging utilizes the endogenous contrast of deoxyhemoglobin under adjustable breathing conditions, avoiding the side effects of tissue retention and toxicity. This work focuses on microimaging of rats' kidneys that are relatively easier to access from the rectum and colon. Future development of MR-compatible endoscope that is robotically controlled [44] will potentially enable dexterous delivery of the WAND through the human rectum. As a rule of thumb, an endo-luminal detector of the size of human colon would be effective for extraluminal region separated from the detector's cylindrical surface by at least the detector's own diameter. Exploiting the proximity between the descending (ascending) colon and the left (right) kidney in humans, the WAND will be particularly useful to image the anterior surface of the kidney. Even though not every clinical scanner has sufficiently large gradient strength to easily obtain 0.1-mm in-plane voxel size, the WAND's sensitivity-enhancement capability will still enable better observation of endogenous signal contrasts at any achievable spatial resolution, paving way for earlier identification of subtle lesions that were too deep inside the abdomen to be sensitively imaged before. For example, as a sensitivity-enhanced endo-luminal MRI detector, the WAND can be used along with endoscopes in patients aged >50 y, for whom recommended routine colonoscopy screening is every 10 years. But unlike conventional endoscopy whose field-of-view is limited to colon epithelium, the WAND's enhanced diagnostic capability for abdominal organs beyond intestinal lumens will be valuable for people who share common risk factors (e.g. age, obesity) for cancer and chronic kidney diseases. For live kidney donors, the WAND may also provide unique ability to discern focal lesions previously undiagnosable by renal biopsy or body fluid biomarkers, prior to costly, high-risk and irreversible donation surgery.

In conclusion, a cylindrically symmetric endo-cavity WAND has been fabricated and non-surgically used inside rat colons to image kidney microstructures and to map hemodynamic responses at high spatial resolution, paving the way for early-stage diagnosis of kidney diseases without the use of contrast agents. When combined with endoscopy, this WAND will potentially enable improved diagnosis on other deep-lying organs from body cavities, such as pancreas (from stomach), and pituitary (from nasal cavities), creating transformative potential to increase the repertoire of diagnostic practice.

Acknowledgment

This work was supported by the National Institutes of Health (grant number R00EB016753), the Department of Radiology of Michigan State University and the MSU Strategic Partnership Grant (grant number 16-SPG-Full-3236). Contents of this paper don't necessarily represent official views of the NIH. The authors declared no conflicts of interest.

References

[1] Z. Milman, J.H. Axelrod, S.N. Heyman, N. Nachmansson, R. Abramovitch, Assessment with unenhanced MRI techniques of renal morphology and hemodynamic changes during acute kidney injury and chronic kidney disease in mice, Am. J. Nephrol. 39 (2014) 268–278.
[2] O.F. Donati, D. Nanz, A.L. Serra, A. Boss, Quantitative BOLD response of the renal medulla to hyperoxic challenge at 1.5 T and 3.0 T, NMR Biomed. 25 (2012) 1133–1138.
[3] L. Li, P. Storey, D. Kim, W. Li, P. Prasad, Kidneys in hypertensive rats show reduced response to nitric oxide synthase inhibition as evaluated by BOLD MRI, J. Magn. Reson. Imaging 17 (2003) 671–675.
[4] H. Lee, K. Mortensen, S. Sanggaard, P. Koch, H. Brunner, B. Quistorff, M. Nedergaard, H. Benveniste, Quantitative Gd-DOTA uptake from cerebrospinal fluid into rat brain using 3D VFA-SPGR at 9.4T, Magn. Reson. Med. 79 (2018) 1568–1578.
[5] S.D. Keilholz, A.C. Silva, M. Raman, H. Merkle, A.P. Koretsky, BOLD and CBV-weighted functional magnetic resonance imaging of the rat somatosensory system, Magn. Reson. Med. 55 (2006) 316–324.
[6] A.I. Holodny, M. Schulder, W.C. Liu, J.A. Maldjian, A.J. Kalnin, Decreased BOLD functional MR activation of the motor and sensory cortices adjacent to a glioblastoma multiforme: implications for image-guided neurosurgery, AJNR Am. J. Neuroradiol. 20 (1999) 609–612.
[7] Y. Liu, X. Mei, J. Li, N. Lai, X. Yu, Mitochondrial function assessed by 31P MRS and BOLD MRI in non-obese type 2 diabetic rats, Physiol. Rep. 4 (2016).
[8] A. Boss, P. Martirosian, M.C. Jehs, K. Dietz, M. Alber, C. Rossi, C.D. Claussen, F. Schick, Influence of oxygen and carbogen breathing on renal oxygenation measured by T2*-weighted imaging at 3.0 T, NMR Biomed. 22 (2009) 638–645.
[9] J.P. O'Connor, J.H. Naish, A. Jackson, J.C. Waterton, Y. Watson, S. Cheung, D.L. Buckley, D.M. McGrath, G.A. Buonaccorsi, S.J. Mills, C. Roberts, G.C. Jayson, G.J. Parker, Comparison of normal tissue R1 and R*2 modulation by oxygen and carbogen, Magn. Reson. Med. 61 (2009) 75–83.
[10] R.A. Jones, M. Ries, C.T. Moonen, N. Grenier, Imaging the changes in renal T1 induced by the inhalation of pure oxygen: a feasibility study, Magn. Reson. Med. 47 (2002) 728–735.
[11] J. Murphyboesch, A.P. Koretsky, An In vivo NMR probe circuit for improved sensitivity, J. Magn. Reson. 54 (1983) 526–532.
[12] S. Eroglu, B. Gimi, B. Roman, G. Friedman, R.L. Magin, NMR spiral surface microcoils: design, fabrication, and imaging, Concept. Magn. Reson. B 17B (2003) 1–10.
[13] M.D. Schnall, C. Barlow, V.H. Subramanian, J.S. Leigh, Wireless implanted magnetic-resonance probes for in vivo NMR, J. Magn. Reson. 68 (1986) 161–167.
[14] D.I. Hoult, B. Tomanek, Use of mutually inductive coupling in probe design, Concepts Magn. Reson. (Magn. Reson. Eng.) 15 (2002) 262–285.
[15] E.D. Wirth 3rd, T.H. Mareci, B.L. Beck, J.R. Fitzsimmons, P.J. Reier, A comparison of an inductively coupled implanted coil with optimized surface coils for in vivo NMR imaging of the spinal cord, Magn. Reson. Med. 30 (1993) 626–633.
[16] M. Decorps, P. Blondet, H. Reutenauer, J.P. Albrand, C. Remy, An Inductively coupled, series-tuned Nmr probe, J. Magn. Reson. 65 (1985) 100–109.
[17] T.H. Farmer, G.A. Johnson, G.P. Cofer, R.R. Maronpot, D. Dixon, L.W. Hedlund, Implanted coil MR microscopy of renal pathology, Magn. Reson. Med. 10 (1989) 310–323.
[18] C. Qian, X. Yu, D.Y. Chen, S. Dodd, N. Bouraoud, N. Pothayee, Y. Chen, S. Beeman, K. Bennett, J. Murphy-Boesch, A. Koretsky, Wireless amplified nuclear MR detector (WAND) for high-spatial-resolution MR imaging of internal organs: preclinical demonstration in a rodent model, Radiology 268 (2013) 228–236.
[19] C. Qian, X. Yu, N. Pothayee, S. Dodd, N. Bouraoud, R. Star, K. Bennett, A. Koretsky, Live nephron imaging by MRI, Am J Physiol Renal Physiol 307 (2014) F1162–1168.
[20] X.C. Zeng, M. Barbic, L. Chen, C.Q. Qian, Sensitive enhancement of vessel wall imaging with an Endo-esophageal Wireless Amplified NMR Detector(WAND), Mag Res Med 78 (2017) 2048–2054.
[21] X. Zeng, L. Chen, C. Wang, J. Wang, C. Qian, Wireless MRI colonoscopy for sensitive imaging of vascular walls, Sci. Rep. 7 (2017) 4228.
[22] X. Zeng, S. Xu, C. Cao, J. Wang, C. Qian, Wireless amplified NMR detector for improved visibility of image contrast in heterogeneous lesions, NMR Biomed. (2018) e3963.
[23] C. Qian, J. Murphy-Boesch, S. Dodd, A. Koretsky, Sensitivity enhancement of remotely coupled NMR detectors using wirelessly powered parametric amplification, Magn. Reson. Med. 68 (2012) 989–996.
[24] L. Xie, K.M. Bennett, C. Liu, G.A. Johnson, J.L. Zhang, V.S. Lee, MRI tools for assessment of microstructure and nephron function of the kidney, Am. J. Physiol. Renal. Physiol. 311 (2016) F1109–F1124.
[25] L.K. Xie, R.E. Cianciolo, B. Hulette, H.W. Lee, Y. Qi, G. Cofer, G.A. Johnson, Magnetic resonance histology of age-related nephropathy in the sprague dawley rat, Toxicol. Pathol. 40 (2012) 764–778.
[26] L. Xie, R. Dibb, G. Cofer, W. Li, P. Nicholls, G. Johnson, C. Liu, Susceptibility tensor imaging of the kidney and its microstructural underpinnings, Mag. Res. Med. 73 (2014) 1270–1281.

[27] L. Xie, M. Sparks, W. Li, Y. Qi, C. Liu, T. Coffman, G. Johnson, Quantitative susceptibility mapping of kidney inflammation and fibrosis in type 1 angiotensin receptor-deficient mice, NMR Biomed. 26 (2013) 1853–1863.
[28] K. Bennett, L. Cullen-Mcwen, V. Puelles, M. Zhang, T. Wu, E. Baldelomar, J. Dowling, J. Charlton, M. Forbes, A. Ng, Q. Wu, J. Armitage, G. Egan, J. Bertram, K. Bennett, MRI-based glomerular morphology and pathology in whole human kidneys, Am. J. Physiol. Renal. Physiol. 306 (2014) F1381–F1390, In Press.
[29] E.J. Baldelomar, J.R. Charlton, S.C. Beeman, B.D. Hann, L. Cullen-McEwen, V.M. Pearl, J.F. Bertram, T. Wu, M. Zhang, K.M. Bennett, Phenotyping by magnetic resonance imaging nondestructively measures glomerular number and volume distribution in mice with and without nephron reduction, Kidney Int. 89 (2016) 498–505.
[30] S.C. Beeman, M. Zhang, L. Gubhaju, T. Wu, J.F. Bertram, D.H. Frakes, B.R. Cherry, K.M. Bennett, Measuring glomerular number and size in perfused kidneys using MRI, Am. J. Physiol. Renal. Physiol. 300 (2011) F1454–F1457.
[31] L. Xie, A.T. Layton, N. Wang, P.E. Larson, J.L. Zhang, V.S. Lee, C. Liu, G.A. Johnson, Dynamic contrast-enhanced quantitative susceptibility mapping with ultrashort echo time MRI for evaluating renal function, Am. J. Physiol. Renal. Physiol. 310 (2016) F174–182.
[32] L. Xie, Y. Qi, E. Subashi, G. Liao, L. Miller-DeGraff, A.M. Jetten, G.A. Johnson, 4D MRI of polycystic kidneys from rapamycin-treated Glis3-deficient mice, NMR Biomed. 28 (2015) 546–554.
[33] C. Baltes, N. Radzwill, S. Bosshard, D. Marek, M. Rudin, Micro MRI of the mouse brain using a novel 400 MHz cryogenic quadrature RF probe, NMR Biomed. 22 (2009) 834–842.
[34] L. Darrasse, J. Ginefri, Perspectives with cryogenic RF probes in biomedical MRI, Biochimie 85 (2003) 915–937.
[35] M.D. Harpen, Sample noise with circular surface coils, Med. Phys. 14 (1987) 616–618.
[36] K.M. Bennett, H. Zhou, J.P. Sumner, S.J. Dodd, N. Bouraoud, K. Doi, R.A. Star, A.P. Koretsky, MRI of the basement membrane using charged nanoparticles as contrast agents, Mag Res Med 60 (2008) 564–574.
[37] M.V. Clavijo Jordan, S.C. Beeman, E.J. Baldelomar, K.M. Bennett, Disruptive chemical doping in a ferritin-based iron oxide nanoparticle to decrease r2 and enhance detection with T1-weighted MRI, Contrast Media Mol. Imaging 9 (2014) 323–332.
[38] E.J. Baldelomar, J.R. Charlton, S.C. Beeman, K.M. Bennett, Measuring rat kidney glomerular number and size in vivo with MRI, Am. J. Physiol. Renal. Physiol. 314 (2018) F399–F406.
[39] L. Bankir, N. Bouby, M.M. Trinh-Trang-Tan, The role of the kidney in the maintenance of water balance, Bailliere's Clin. Endocrinol. Metabol. 3 (1989) 249–311.
[40] L. Bankir, C. de Rouffignac, Urinary concentrating ability: insights from comparative anatomy, Am. J. Physiol. 249 (1985) R643–666.
[41] W. Kriz, Structural organization of the renal medulla: comparative and functional aspects, Am. J. Physiol. 241 (1981) R3–16.
[42] L.R. Bigongiari, S.K. Patel, H. Appelman, J.R. Thornbury, Medullary rays Visualization during excretory urography, Am. J. Roentgenol., Radium Therapy, Nucl. Medi. 125 (1975) 795–803.
[43] L.P. Li, J. Lu, Y. Zhou, M.V. Papadopoulou, T. Franklin, U. Bokhary, R. Solomon, A. Sen, P.V. Prasad, Evaluation of intrarenal oxygenation in iodinated contrast-induced acute kidney injury-susceptible rats by blood oxygen level-dependent magnetic resonance imaging, Invest. Radiol. 49 (2014) 403–410.
[44] Y. Chen, K.W. Kwok, Z.T. Tse, An MR-conditional high-torque pneumatic stepper motor for MRI-guided and robot-assisted intervention, Ann. Biomed. Eng. 42 (2014) 1823–1833.
[45] C.H. Cunningham, J.M. Pauly, K.S. Nayak, Saturated double-angle method for rapid B-1 plus mapping, Magn. Reson. Med. 55 (2006) 1326–1333.